A Case Study on Atlantic Tropical Cyclogenesis and Saharan Air Layer Simulated Using WRF/Chem Coupled with an AOD Data Assimilation System

Zhiquan Liu and Dan Chen

National Center for Atmospheric Research, Boulder, Colorado, USA

Abstract

This study investigated the dust radiative effects on tropical cyclogenesis and the Saharan Air Layer (SAL) over the Atlantic Ocean by using the Gridpoint Statistical Interpolation three-dimensional variational data assimilation (DA) system coupled with the Weather Research and Forecasting/Chemistry model. Two experiments were conducted with (DA) and without (NO_DA) the assimilation of MODIS 550-nm aerosol optical depth (AOD) retrievals. One-week (from 28 August to 5 September, 2006) assimilation of MODIS AOD substantially improved the depiction of Saharan dust outbreak and transport feature. Differences of 180-hr forecasts initiated at 00 UTC 5 September from the two experiments were analyzed to evaluate the dust radiative effects. The dust-radiation interaction over mostly cloudless condition in the first 3-day model simulation mainly warmed the dusty layer and the layer near the surface via dominated dust absorption effect of shortwave solar radiation. At a later stage of forecasts (Sep. 9-11) with cloudier conditions and more pronounced semi-direct impact, the Meso-sclae Convective Systems (MCS) have developed over time in the Main Cyclogenesis Region with significant temperature increase and relative humidity decrease in the middle troposphere when assimilating AOD. This suppressed clouds and precipitation and enhanced downward motion and atmospheric stability, which finally resulted in the erosion of spurious MCSs appeared in the NO_DA experiment. Due to early suppression, more ice precipitation and high clouds were formed as more water ascended to freezing levels, and the greater amount of freezing water aloft released extra latent heat and invigorated the convection in peripheral region. The storm was further weakened by the bled and cooled low-level airflow caused by peripheral clouds invigoration. Near the end of 180-hr forecast from the AOD DA experiment, the hotness and dryness features of the SAL were more pronounced when compared to the NO_DA experiment and likely reflected a more realistic model simulation of dust-radiative effects.

1. Introduction

Mineral dust, one of the most abundant aerosol species in the atmosphere, has important weather and climatic effects through its influence on solar and terrestrial radiation and the radiative and physical properties of clouds [e.g., Sokolik et al., 1999; Ginoux et al., 2001; Ramanathan et al., 2001; Lau et al., 2009; Zhao et al., 2010]. The Sahara desert over North Africa is the largest source of mineral dust in the world. During the summer months, Saharan dust outbreaks are associated with a dry and hot well-mixed layer (Saharan Air Layer, SAL) extending from 1500 m to 6000 m over the North Atlantic Ocean. Several studies have examined the Saharan dust radiative effects on the SAL and environment shear [e.g., Chen et al., 2010; Zhao et al., 2010]. For dust plumes under cloudless conditions over the eastern Atlantic Ocean, the radiative effect is dominated by the dust shortwave radiation interaction, resulting in net heating with the maximum occurring slightly below the peak dust concentration. High aerosol optical depth (AOD) below 700 hPa is associated with increased atmospheric stability through increased temperature and dryness. Thus in addition to the hot air that originates from the desert upstream, the dust-induced radiative forcing helps the SAL to retain the warmness and dryness throughout its depth as it is carried as far as the western Caribbean Sea.

Saharan dust, often propagating downstream along SAL to the Atlantic Ocean, can modify the SAL and its environment by changing the energy budget through direct, semi-direct and indirect effects [e.g., Chen et al., 2010; Su et al., 2008; Zhao et al., 2010]. Tropical cyclones (TCs) in the Atlantic basin often develop from meoscale convective systems (MCSs) embedded within African easterly waves (AEWs) that originate over West Africa [Landsea, 1993]. Near the southern boundary of SAL, the dusty, hot and dry air is associated with AEWs, which can affect TC activity. In cloudy conditions where relatively cool and moist marine air undercuts the SAL as it moves westward, the dust can affect clouds through semi-direct thermodynamic process or indirect cloud microphysical processes. Several observational and numerical studies [e.g., Karyampudi and Carlson, 1988; Karyampudi and Pierce, 2002; Dunion and Velden, 2005; Evan et al., 2006; Jones et al., 2007; Wu, 2007; Shu and Wu, 2009; Sun et al., 2008, 2009; Partt and Evans, 2009; Reale et al, 2009, Chen et al., 2010] have shown evidence for aerosol-induced intensification and weakening of TC development. For example, by using satellite data Dunion and Velden [2005] found that the dry SAL can suppress Atlantic TC activity by increasing the vertical wind shear and stabilizing the environment at low atmospheric levels. They also suggested that convectively driven downdrafts caused by the SAL dry air can be an important inhibiting factor for TCs.

To accurately forecast TC intensity, research activities and field experiments have also examined tropical cyclogenesis [Zipser et al., 2009]. Tropical cyclogenesis is strongly influenced by environmental factors, such as the sea surface temperature, moisture in the lower troposphere and vertical wind shear [Gray, 1968]. Sun et al. [2009] and Wu et al. [2007] incorporated the Atmospheric Infrared Sounder (AIRS) measured temperature and humidity

profiles into numerical weather prediction models (WRF and MM5 respectively), to study the effects of SAL on TC activity. Both of them found that with the assimilation of AIRS observations during dust outbreak periods, the dry and warm SAL was better simulated such that the development of tropical disturbances was inhibited along the southern edge of the SAL. In their studies, the effects on TC development were investigated from the view of SAL.

The magnitude of the radiative impact of dust highly depends upon the distribution of the dust concentration and its optical characteristics. While the modeling of the spatial distribution of Saharan dust and its optical depth remains uncertain and challenging, AOD data assimilation (DA), combining satellite derived AOD observations with numerical model output, has proved to be skillful at improving aerosol and AOD forecasts [Collins et al., 2001; Liu et al., 2011]. Liu et al. [2011] implemented AOD DA within the National Centers for Environmental Prediction (NCEP) Gridpoint Statistical Interpolation (GSI) three-dimensional variational (3DVAR) DA system coupled to the Goddard Chemistry Aerosol Radiation and Transport (GOCART) [Chin et al., 2000, 2002] aerosol scheme within the Weather Research and Forecasting/Chemistry (WRF/Chem) model [Grell et al., 2005]. Their results demonstrated improved aerosol forecasts from AOD DA over a week-long period while studying a dust storm event over East Asia.

In this study, we will investigate the dust-radiation effects on SAL and TC genesis in the Atlantic Ocean using the GSI-WRF/Chem coupled AOD DA system. The Atlantic TC case and motivation are presented in section 2, followed by model description and experimental design in section 3. Model simulation results are described in section 4 and conclusions are given in section 5.

2. Case and Motivation

We selected the same period as in Sun et al. [2009], which spanned Sep. 5-12, 2006. AIRS retrievals of vertical temperature (T) and relative humidity (RH) profiles showed the clear feature of SAL - 1-4 K higher T and 50% lower RH in the low-middle atmosphere (e.g., 850-700 hPa) of the heavy dusty area (dust AOD > 0.4).

It is likely that higher T observed by AIRS in the heavy dust area was induced by dust radiative effects. In this study, we attempt to investigate three questions: 1. Can the feature of the Saharan dust outbreak be well simulated by assimilating MODIS AOD observations? 2. How does dust affect TC development through radiative effects? Can the TC suppression be reproduced as in Sun et al [2009]? 3. Can the dry and warm SAL be better simulated with the assimilated dust field? To the authors' knowledge, this is the first study to investigate the TC genesis and SAL using the WRF/Chem model.

3. Model Description and Experimental Design

Version 3.4.1 of WRF/Chem was used with "online" coupled meteorological and chemical processes. The model domain with 36-km horizontal grid spacing covers the Atlantic Ocean and Sahara desert (Fig. 1). There are 57 vertical levels extending from the surface to 10 hPa. Aerosol direct and semi-direct effects are allowed in WRF/Chem by linking the optical properties of GOCART aerosols (OC and BC with 2 size bins, sulfate, dust with 5 size bins and sea salt with 4 size bins) to the Goddard Space Flight Center Shortwave radiation scheme [Chou and Suarez, 1994]. Aerosol indirect effects were not implemented for GOCART with the WRF/Chem version used. The WRF single-moment 6-class microphysics scheme and the Grell-Devenyi ensemble cumulus parameterization [Grell and Devenyi, 2002] were used. The dust emission flux is computed as a function of probability source function and surface wind speed [Ginoux et al., 2001]. Similar to dust uplifting, sea salt emissions from the ocean are highly dependent on the surface wind speed and calculated as a function of wind speed at 10 m and sea salt particle radius [Chin et al., 2002]. The lateral boundary conditions (LBCs) for meteorological fields were provided by the NCEP GFS forecasts. LBCs for chemistry/aerosol fields were idealized profiles embedded within the WRF/Chem model and represented clean oceanic conditions (could cite Schwartz et al. [2012] if you wanted).

NCEP's GSI 3DVAR DA system was used to assimilate total 550-nm AOD (hereafter "AOD") retrievals from MODIS sensors onboard Terra and Aqua satellites, as described in Liu et al. [2011]. MODIS AOD retrievals of Deep Blue products over desert [Hsu et al., 2004] and dark targeting products over ocean and vegetated land [Remer et al., 2005] were assimilated in this study. GSI 3DVAR system calculates a best-fit "analysis" considering the observations (AOD in our case) and background fields (short-term WRF/Chem forecasts in our case) weighted by their error characteristics. The community radiative transfer model (CRTM) [Han et al., 2006; Liu and Weng, 2006] is used as the AOD observation operator in GSI to transform the GOCART aerosol profiles into AOD. Each 3-D aerosol species is used as analysis variables of 3DVAR, and the 3-D mass concentrations of the aerosol species are analyzed in a one-step minimization procedure constrained by the observation and background error covariances (BECs). The AOD observation error is assumed to be spatially uncorrelated and modeled as in Liu et al. [2011]. To more accurately reflect the dust-dominated feature, the BEC statistics for each aerosol variable were calculated by utilizing the "NMC method" [Parrish and Derber, 1992] based upon one-month of WRF/Chem forecasts for the dust outbreak month of August 2005. Standard deviations and horizontal/vertical correlation lengthscales of the background errors (separated for each aerosol species) were calculated using the method described by Wu et al. [2002]. Further details regarding the AOD DA system, including the algorithm, observation operator, and modeling of the background and observation error covariances can be found in Liu et al. [2011].

Two experiments were conducted using this coupled GSI-WRF/Chem system with (DA) and without (NO_DA) assimilating MODIS AOD observations. Both experiments initialized a 6-hr WRF/Chem forecast every 6-hr starting from 00 UTC 28 August 2006. Meteorological

initial conditions (ICs) for each forecast came from GFS analyses. For NO_DA, aerosol fields were simply carried over from cycle to cycle (similar to a continuous aerosol forecast). For DA, GSI 3DVAR updated GOCART aerosol variables by assimilating MODIS AOD at 12 UTC and 18 UTC (when AOD observations were available) using the previous cycle's 6-hr forecast as the background. A final analysis was made at 00 UTC 5 September from this 6 hourly cycling procedure and then a 180-hr forecast was initialized for both experiments. Note that meteorological ICs in the two 180-hr forecasts are the same (from the GFS analysis) and the forecast differences of meteorological fields are resulted solely from the differences of aerosol ICs between the DA and NO_DA experiments. We now present results from the two 180-hr forecasts.

4. Results

4.1 Assimilated Dust Outbreak

After a one-week period (00 UTC 28 August – 00 UTC 5 September) for aerosol spin-up, the impact of AOD DA on the depiction of the dust outbreak event can be clearly seen in Figure 1, which shows the spatial distribution of AOD valid at 00 UTC 5 September from the NO_DA and DA experiments. The ratio of dust contributed AOD is also shown as red contour lines. While the NO_DA experiment substantially underpredicted aerosol concentrations, particularly over the Atlantic Ocean, the DA experiment produced much larger AOD values than the NO_DA experiment not only in the dust source region but also over the Atlantic Ocean (~1.3 vs. ~0.25 for the maximum values). In the DA experiment, the high AOD values extended westward to 60° W and spanned about 10-30 degrees in latitude off the coast of northern Africa. While the dust AOD ratios over ocean reached as high as 0.8 in the DA experiment, clearly indicating a dust-dominated event, the NO_DA experiment had the dust AOD ratios less than 0.4 over ocean, significantly underpredicting the dust outbreak. The feature in the DA experiment is consistent with the OMI Aerosol Index images shown in Sun et al. [2009].

Note that only column-total 550-nm AOD was assimilated and no aerosol speciation information was contained in observations. It is important to have the phenomena-specific background error statistics to allow an appropriate adjustment of individual aerosol species during assimilation. These error statistics were obtained using the WRF/Chem forecasts for the dust outbreak month of August 2005. Consistent with the dust outbreak period, the standard deviations of dust errors are one- or two-orders of magnitude larger than those of other species (not shown). Larger background errors of dust allowed larger adjustments of the dust field, which is crucial for the aerosol analyses of the Sahara dust outbreak period in this study.

4.2 Impact on Tropical Cyclogenesis

As our main goal is to investigate the dust-radiative effects on TC development in the 180-h forecasts initialized from 00 UTC 5 September, a small region (black rectangle in Fig. 1b) defined as Main Cyclogenesis Region (MCR), where TCs often develop as the dust resided, is ideal for a detailed analysis of results. As TCs in the Atlantic basin often develop from MCSs embedded within AEWs, cloud water and convective precipitation are good indicators of MCSs. The Eastern Atlantic Ocean was mostly under cloudless conditions in the first 48-hr forecasts (not shown). The convective system developed over time and obvious clouds occurred after 8 September.

Figure 2 shows the MCR-averaged differences of AOD, vertical velocity, T, RH, cloud liquid and cloud ice water as a function of height and forecast valid time between the two experiments (DA – NO_DA). The time series started from 00 UTC Sep 5. The largest AOD increase due to dust outbreak occurred at 600-950 hPa. The 180-hr forecast can be divided into two periods with mostly cloudless or cloudy conditions, respectively. For the first 3-4 days (Sep. 5-8) when MCR was under cloudless or partly cloudy conditions, dust-radiation interaction was mostly through direct effects combining both shortwave and longwave radiation processes. In general, dust absorption of shortwave radiation creates a heating effect around the dust maxima, and dust extinction (absorption and scattering) of shortwave radiation reduces the downward radiative flux, thus leading to a cooling effect below the dusty layer. For longwave radiation, dust absorbs and reflects energy from below and then re-emits longwave radiation in all directions, yielding a cooling effect in the dusty layer and a warming effect near the surface. It can be seen from Figure 2c that within the dusty layer the net heating effect resulted from the dominated shortwave absorption, whereas the net warming near the surface was caused by the dominated longwave radiation [Carlson and Benjamin, 1980; Zhu et al., 2007; Wong et al., 2009; Chen et al., 2010].

Over time, MCSs developed and the MCR was under cloudier condition from Sep. 9 as deep and moist convection was triggered by persistent lower tropospheric convergence associated with pre-existing disturbances. When dust interacted with clouds, the clouds significantly influence the direct and semi-direct radiative impacts of dust [Su et al., 2008; Quijano et al, 2000] and the aerosol-induced warming due to semi-direct effect of dust is much more pronounced than direct effect [Su et al., 2008]. This caused larger temperature increase in the middle troposphere from 12 UTC 10 September. The increased temperature below 600 hPa led to more stable atmosphere and suppressed the convection [Wong and Dessler , 2005; Wong et al., 2009], as evidenced by decreased upward vertical velocity for Sep. 9-11 (Figure 2b). The dust also evaporated low-level clouds through semi-direct effect [Grassl, 1975]. However, starting from ~12 UTC 11 September, the MCR-averaged vertical velocity and clouds were increased. We thus further divide the cloudy period into two phases: before and after 12 UTC 11 September. For each phase, we select one time step model output to analyze in detail the dust effects to TC development.

Figure 3 shows the spatial distribution of column-integrated CLWP valid at 00 UTC 10 September and 114-hr~120-hr accumulated convective precipitation in the MCR. Figure 4 displays the 10-m winds overlaid with 850-hPa potential temperature at the same time. Three MCSs occurred in NO_DA, but MCS A centered at (20º N, 45º W) disappeared in DA. The differences between the two experiments (right panels in Figures 4) show significant decrease of cloud and convective rain at the location of the MCS A. That was mainly due to the dust-induced evaporative effects. As indicated in many previous studies (e.g., Leary and Houze, 1979; Brown, 1979; Sun et al., 2009), evaporative and melting cooling can create negative buoyancy and would induce meso-scale downdrafts. Figure 5 depicts the west-east cross sections across the center of MCS A (red dashed line in Figure 4). Figures 5a,b are the (u, 100 ×vertical wind speed) vectors and potential temperature from DA and NO_DA respectively. Figures 5c,d are the differences of potential temperature and RH between the two experiments (DA-NO_DA). The differences of (u, 100×w) vectors (overlaid in Figure 5c) show enhanced downward motion and a cold pool around the center of MCS A at ~44º W. ~5-K potential temperature decrease and 80% relative humidity decrease occurred in the middle troposphere where MCS A was located. The enhanced downdraft stabilized the boundary layer and weakened the large-scale boundary layer convergence, which drives the deep and moist convection. Over time, these processes resulted in the erosion of the MCS. The surface wind speed around the MCS A (Figure 4) decreased by ~10 m/s. This disturbance suppression is very similar to the WRF simulations with AIRS temperature assimilation in Sun et al. [2009].

Figures 6-8 are the same as Figures 3-5 but for the forecast valid at 00 UTC 12 September. Similar to the suppression of the MCS A at 00 UTC 10 September, the MCS D (centered at 16º N, 45º W) disappeared in DA with a large decrease of potential temperature and RH (Figure 8a,b). The MCS E retained in DA but shifted a little bit northward (Figure 7). However, the spatial distributions of CLWP and convective rainfall (Figure 6) show not only significant decrease at the centers of the MCSs but also obvious increases in the peripheral region (e.g., from the DA experiment, stronger rain band in the south of MCS D location). The cross sections at MCS E also shows stronger convection in the peripheral region. Jenkins et al. [2008] found the linkage between Saharan dust and invigoration of TC convective rain bands by using satellite imagery and rawinsondes. The enhanced cloud water content and cloud- and precipitation-sized particles associated with tropical cyclogenesis were observed just south of the SAL during the NASA African Monsoon Multidisciplinary Analysis (NAMMA) campaign (August-September 2006) in the Eastern Atlantic. Rosenfeld et al. [2012] also used satellite observations and found that aerosols present in the peripheral clouds of the TC slow the rain-forming processes there, invigorates the convection in peripheral region later, and decrease the TC maximum wind speed. Consistent with the observations in Koren et al. [2005] and Rosenfeld et al. [2012], more liquid and ice clouds in the higher layers (around 00 UTC 12 September in Figure 2d) were invigorated in the DA experiment, because more water can ascend to freezing levels as supercooled water due to early suppression.

7

Besides, the increased upward vertical velocity (Figure 2b) is also evident. According to the conceptual model in Rosenfeld et al. [2012], the greater vigor of the peripheral clouds draws more ascending air at the periphery of the storm (indicated by the strong winds between 12-14º N, 35-45º W in Figure 7a), thereby bleeding the low-level airflow toward the storm center D. In addition, the intensified ice precipitation in the peripheral clouds melted and evaporated at the lower levels, thereby cooling the air that converges into the center (cool pool at 45º W in Figure 8c). The cooler air has less buoyancy and hence dampens the rising air in the storm center, thereby further weakening the convergence and the maximum wind speed of the storm.

In Sun et al. [2009], after the assimilation of AIRS temperature in the WRF simulations the TC disturbances were also suppressed for the same event. Their analysis showed that the major reason for disturbance suppression is the better-simulated warm and dry SAL features. They found that the thermal structure of the SAL led to low-level temperature inversion and increased stability and vertical wind shear, which play direct roles to the TC suppression. They also found the warm SAL temperature may also play the indirect effects by increasing evaporative cooling and initiating mesoscale downdrafts. Their explanations were consistent for the disappearance of MCS A in our AOD DA experiment. The difference is that they assimilated AIRS temperature to improve meteorological ICs, whereas we assimilated MODIS AOD to improve the dust ICs and thus alter subsequent TC forecast via direct and semi-direct dust-radiative feedback effects. In Sun et al. [2009], the WRF forecasts only last for 96 hours and no dust radiative effects were considered, thus the later invigoration was not reported.

4.3 Impact on SAL

Saharan dust, often propagating downstream along SAL to the Atlantic Ocean, can also modify SAL by changing the energy budget through direct and semi-direct radiative effects. In our two 180-hr forecasts initialized from the same meteorological ICs, the meteorological differences in the two forecasts were all due to dust-radiative effects. As shown in Figure 2, there are obvious T and RH changes when dust interacted with clouds through semi-direct effects after Sep. 10. Figure 9 shows the spatial distributions of 850 hPa T and 700 hPa RH, from the two experiments as well as the corresponding difference fields (DA-NO_DA) for one-week forecast valid at 00 UTC 12 September. The tongue shape of the warm and dry SAL extended more westward in DA with ~5 degree T increase and 70% RH decrease over the Eastern Atlantic. Figure 12 displays the west-east cross sections of T and RH differences along the black solid line in Figure 10.

5. Conclusions

In this study, the GSI/WRF-Chem coupled AOD DA system was used to investigate the dust-radiative effects on tropical cyclogenesis and SAL over the Atlantic Ocean during a Saharan dust outbreak event on Sep. 5-12, 2006. Prior to 180-hr forecasts initialized from 00 UTC 5

September, two 6-hourly cycling experiments with (DA) and without (NO_DA) assimilation of MODIS 550-nm AOD were conducted from 00 UTC 28 August to 00 UTC 5 September. One week AOD DA substantially improved the depiction of dust outbreak and transport, with maximum AOD increased from ~0.25 (in NO_DA) to ~1.3 (in DA) over the Atlantic Ocean at 00 UTC 5 September. In addition, the assimilated dust-contributed AOD ratio in total AOD was increased from < 0.4 to > 0.8. The better-analyzed dust outbreak features were consistent with the OMI Aerosol Index images and allowed a more realistic model simulation of dust radiative effects.

180-hr forecasts were then initialized from 00 UTC 5 September for the two experiments with different aerosol ICs but the same meteorological ICs interpolated from the GFS analysis. In the Main Cyclogenesis Region (MCR) over ocean during the mostly cloudless period (Sep. 5-7), the air was maximally heated at 600-850 hPa levels because of the dominated dust-absorption effect of shortwave solar radiation. Another local heating was found in the lower boundary layer due to the dominance of downward longwave radiation emitted from dusty layer. After Sep. 9, MCSs formed. Dust semi-direct effect induced much larger T increase and RH decrease in the middle troposphere within the MCR, where the warm air enhanced the static stability, suppressed convection and evaporated clouds during the subsequent two days (Sep. 9-10). These changes to clouds and precipitation further resulted in T decrease and RH increase in the lower troposphere (below 850 hPa).

In the first few days of MCS development, the warm anomaly induced by dust semi-direct radiative effect suppressed clouds and precipitation in the high AOD region and enhanced downward motion, and a cold pool occurred at the storm center on Sep 9-10. ~5 degrees potential temperature decrease and 80% RH decrease occurred in the middle troposphere. Because the same meteorological ICs were used in both DA and NO_DA experiments and dust radiative feedback took time to be in effect, the warmness and dryness features of SAL from the AOD DA experiment were more evident at later stages of the 180-hr forecast. An up to 7-degree T increase and 80% RH decrease at 600-850 hPa were reached for the forecast valid at 00 UTC 12 September. However, a coupled MET plus aerosol DA [Schwartz et al., 2014], which simultaneously assimilates meteorological and AOD observations, is expected to better reveal SAL features in the earlier stage of the forecast. This will be further explored in the future with possibly more case studies in order to draw more general conclusions.

Reference

Brown, J. M. (1979), Mesoscale Unsaturated Downdrafts Driven by Rainfall Evaporation - Numerical Study, J Atmos Sci, 36(2), 313-338.
Carlson, T. N., and S. G. Benjamin (1980), Radiative Heating Rates for Saharan Dust, J Atmos Sci, 37(1), 193-213.
Chen, S. H., S. H. Wang, and M. Waylonis (2010), Modification of Saharan air layer and environmental shear over the eastern Atlantic Ocean by dust-radiation effects, J Geophys Res-Atmos, 115.

Chin, M., D. L. Savoie, B. J. Huebert, A. R. Bandy, D. C. Thornton, T. S. Bates, P. K. Quinn, E. S. Saltzman, and W. J. De Bruyn (2000), Atmospheric sulfur cycle simulated in the global model GOCART: Comparison with field observations and regional budgets, J Geophys Res-Atmos, 105(D20), 24689-24712.

Chin, M., P. Ginoux, S. Kinne, O. Torres, B. N. Holben, B. N. Duncan, R. V. Martin, J. A. Logan, A. Higurashi, and T. Nakajima (2002), Tropospheric aerosol optical thickness from the GOCART model and comparisons with satellite and Sun photometer measurements, J Atmos Sci, 59(3), 461-483.

Chou, M.-D., and M.J. Suarez (1994), An efficient thermal infrared radiation parameterization for use in general circulation models, NASA Tech. Memo., TM 104606, vol. 3, 25 pp., NASA Goddard Space Flight Cent., Greenbelt, Md.

Collins, W. D., P. J. Rasch, B. E. Eaton, B. V. Khattatov, J. F. Lamarque, and C. S. Zender (2001), Simulating aerosols using a chemical transport model with assimilation of satellite aerosol retrievals: Methodology for INDOEX, J Geophys Res-Atmos, 106(D7), 7313-7336.

Dunion, J. P., and C. S. Velden (2004), The impact of the Saharan air layer on Atlantic tropical cyclone activity, B Am Meteorol Soc, 85(3), 353-+.

Evan, A. T., J. Dunion, J. A. Foley, A. K. Heidinger, and C. S. Velden (2006), New evidence for a relationship between Atlantic tropical cyclone activity and African dust outbreaks, Geophys Res Lett, 33(19).

Ginoux, P., M. Chin, I. Tegen, J. M. Prospero, B. Holben, O. Dubovik, and S. J. Lin (2001), Sources and distributions of dust aerosols simulated with the GOCART model, J Geophys Res-Atmos, 106(D17), 20255-20273.

Gray, W. M. (1968), Global View of Origin of Tropical Disturbances and Storms, Mon Weather Rev, 96(10), 669-&.

Grassl, H.(1975), Albedo Reduction and Radiative Heating of Clouds by Absorbing Aerosol Particles, Contrib. Atmos. Phys., 48, 199–210

Grell, G. A., and D. Devenyi (2002), A generalized approach to parameterizing convection combining ensemble and data assimilation techniques, Geophys Res Lett, 29(14).

Grell, G. A., S. E. Peckham, R. Schmitz, S. A. McKeen, G. Frost, W. C. Skamarock, and B. Eder (2005), Fully coupled "online" chemistry within the WRF model, Atmos Environ, 39(37), 6957-6975.

Han, Y., P. van Delst, Q. Liu, F. Weng, B. Yan, R. Treadon, and J. Derber (2006), JCSDA Community Radiative Transfer Model (CRTM)- Version 1, NOAA Tech. Rep. NESDIS 122, 33 pp., NOAA Silver Spring, Md.

Hsu, N. C., S. C. Tsay, M. D. King, and J. R. Herman (2004), Aerosol properties over bright-reflecting source regions, Ieee T Geosci Remote, 42(3), 557-569.

Hsu, N. C., S. C. Tsay, M. D. King, and J. R. Herman (2004), Aerosol properties over bright-reflecting source regions, Ieee T Geosci Remote, 42(3), 557-569.

Jenkins, G. S., A. S. Pratt, and A. Heymsfield (2008), Possible linkages between Saharan dust and tropical cyclone rain band invigoration in the eastern Atlantic during NAMMA-06, Geophys Res Lett, 35(8).

Jones, T. A., D. J. Cecil, and J. Dunion (2007), The environmental and inner-core conditions governing the intensity of Hurricane Erin (2001), Weather Forecast, 22(4), 708-725.

Karyampudi, V. M., and T. N. Carlson (1988), Analysis and Numerical Simulations of the Saharan Air Layer and Its Effect on Easterly Wave Disturbances, J Atmos Sci, 45(21), 3102-3136.

Karyampudi, V. M., and H. F. Pierce (2002), Synoptic-scale influence of the Saharan air layer on tropical cyclogenesis over the eastern Atlantic, Mon Weather Rev, 130(12), 3100-3128.

Koren, I., Y. J. Kaufman, D. Rosenfeld, L. A. Remer, and Y. Rudich (2005), Aerosol invigoration and restructuring of Atlantic convective clouds, Geophys Res Lett, 32(14).

Landsea, C. W. (1993), A Climatology of Intense (or Major) Atlantic Hurricanes, Mon Weather Rev, 121(6), 1703-1713.

Lau, K. M., K. M. Kim, Y. C. Sud, and G. K. Walker (2009), A GCM study of the response of the atmospheric water cycle of West Africa and the Atlantic to Saharan dust radiative forcing, Ann Geophys-Germany, 27(10), 4023-4037.

Leary, C. A., and R. A. Houze (1979), Melting and Evaporation of Hydrometeors in Precipitation from the Anvil Clouds of Deep Tropical Convection, J Atmos Sci, 36(4), 669-679.

Liu, Q. H., and F. Z. Weng (2006), Advanced doubling-adding method for radiative transfer in planetary atmospheres, J Atmos Sci, 63(12), 3459-3465.

Liu, Z. Q., Q. H. Liu, H. C. Lin, C. S. Schwartz, Y. H. Lee, and T. J. Wang (2011), Three-dimensional variational assimilation of MODIS aerosol optical depth: Implementation and application to a dust storm over East Asia, J Geophys Res-Atmos, 116.

Parrish, D. F., and J. C. Derber (1992), The National-Meteorological-Centers Spectral Statistical-Interpolation Analysis System, Mon Weather Rev, 120(8), 1747-1763.

Pratt, A. S., and J. L. Evans (2009), Potential Impacts of the Saharan Air Layer on Numerical Model Forecasts of North Atlantic Tropical Cyclogenesis, Weather Forecast, 24(2), 420-435.

Quijano, A. L., I. N. Sokolik, and O. B. Toon (2000), Radiative heating rates and direct radiative forcing by mineral dust in cloudy atmospheric conditions, J Geophys Res-Atmos, 105(D10), 12207-12219.

Ramanathan, V., P. J. Crutzen, J. T. Kiehl, and D. Rosenfeld (2001), Atmosphere - Aerosols, climate, and the hydrological cycle, Science, 294(5549), 2119-2124.

Reale, O., W. K. Lau, K. M. Kim, and E. Brin (2009), Atlantic Tropical Cyclogenetic Processes during SOP-3 NAMMA in the GEOS-5 Global Data Assimilation and Forecast System, J Atmos Sci, 66(12), 3563-3578.

Remer, L. A., et al. (2005), The MODIS aerosol algorithm, products, and validation, J Atmos Sci, 62(4), 947-973.

Remer, L. A., et al. (2005), The MODIS aerosol algorithm, products, and validation, J Atmos Sci, 62(4), 947-973.

Rosenfeld, D., W. L. Woodley, A. Khain, W. R. Cotton, G. Carrio, I. Ginis, and J. H. Golden (2012), Aerosol Effects on Microstructure and Intensity of Tropical Cyclones, B Am Meteorol Soc, 93(7), 987-1001.

Schwartz, C. S., Z. Q. Liu, H. C. Lin, and S. A. McKeen (2012), Simultaneous three-dimensional variational assimilation of surface fine particulate matter and MODIS aerosol optical depth, J Geophys Res-Atmos, 117.

Shu, S. J., and L. G. Wu (2009), Analysis of the influence of Saharan air layer on tropical cyclone intensity using AIRS/Aqua data, Geophys Res Lett, 36.

Sokolik, I. N., O. B. Toon, and R. W. Bergstrom (1998), Modeling the radiative characteristics of airborne mineral aerosols at infrared wavelengths, J Geophys Res-Atmos, 103(D8), 8813-8826.

Su, J., J. P. Huang, Q. Fu, P. Minnis, J. M. Ge, and J. R. Bi (2008), Estimation of Asian dust aerosol effect on cloud radiation forcing using Fu-Liou radiative model and CERES measurements, Atmos Chem Phys, 8(10), 2763-2771.

Su, J., J. P. Huang, Q. Fu, P. Minnis, J. M. Ge, and J. R. Bi (2008), Estimation of Asian dust aerosol effect on cloud radiation forcing using Fu-Liou radiative model and CERES measurements, Atmos Chem Phys, 8(10), 2763-2771.

Sun, D. L., K. M. Lau, and M. Kafatos (2008), Contrasting the 2007 and 2005 hurricane seasons: Evidence of possible impacts of Saharan dry air and dust on tropical cyclone activity in the Atlantic basin, Geophys Res Lett, 35(15).

Sun, D. L., W. K. M. Lau, M. Kafatos, Z. Boybeyi, G. Leptoukh, C. W. Yang, and R. X. Yang (2009), Numerical Simulations of the Impacts of the Saharan Air Layer on Atlantic Tropical Cyclone Development, J Climate, 22(23), 6230-6250.

Wong, S., and A. E. Dessler (2005), Suppression of deep convection over the tropical North Atlantic by the Saharan Air Layer, Geophys Res Lett, 32(9).

Wong, S., A. E. Dessler, N. M. Mahowald, P. Yang, and Q. Feng (2009), Maintenance of Lower Tropospheric Temperature Inversion in the Saharan Air Layer by Dust and Dry Anomaly, J Climate, 22(19), 5149-5162.

Wu, W. S., R. J. Purser, and D. F. Parrish (2002), Three-dimensional variational analysis with spatially inhomogeneous covariances, Mon Weather Rev, 130(12), 2905-2916.

Wu, W. S., R. J. Purser, and D. F. Parrish (2002), Three-dimensional variational analysis with spatially inhomogeneous covariances, Mon Weather Rev, 130(12), 2905-2916.

Wu, L. G. (2007), Impact of Saharan air layer on hurricane peak intensity, Geophys Res Lett, 34(9).

Zhao, C., X. Liu, L. R. Leung, B. Johnson, S. A. McFarlane, W. I. Gustafson, J. D. Fast, and R. Easter (2010), The spatial distribution of mineral dust and its shortwave radiative forcing over North Africa: modeling sensitivities to dust emissions and aerosol size treatments, Atmos Chem Phys, 10(18), 8821-8838.

Zhu, A., V. Ramanathan, F. Li, and D. Kim (2007), Dust plumes over the Pacific, Indian, and Atlantic oceans: Climatology and radiative impact, J Geophys Res-Atmos, 112(D16).

Zipser, E. J., et al. (2009), The Saharan Air Layer and the Fate of African Easterly Waves, B Am Meteorol Soc, 90(8), 1137-1156.
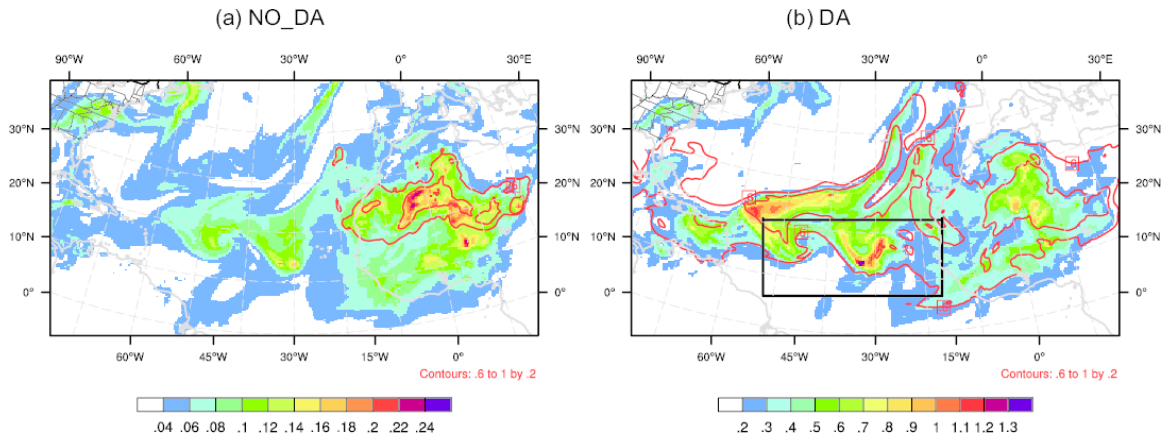
Figure 1. After one-week period (28 August – 5 September 2006) for aerosol spin-up, total 550-nm AOD distribution valid at 00 UTC 5 Sep. 2006 from the (a) NO_DA and (b) DA experiments. Also shown are dust AOD ratios in red contours. Note that color scales are intentionally made different between NO_DA and DA for a better visualization. Black rectangle in (b) is defined as the Main Cyclogenesis Region (MCR).
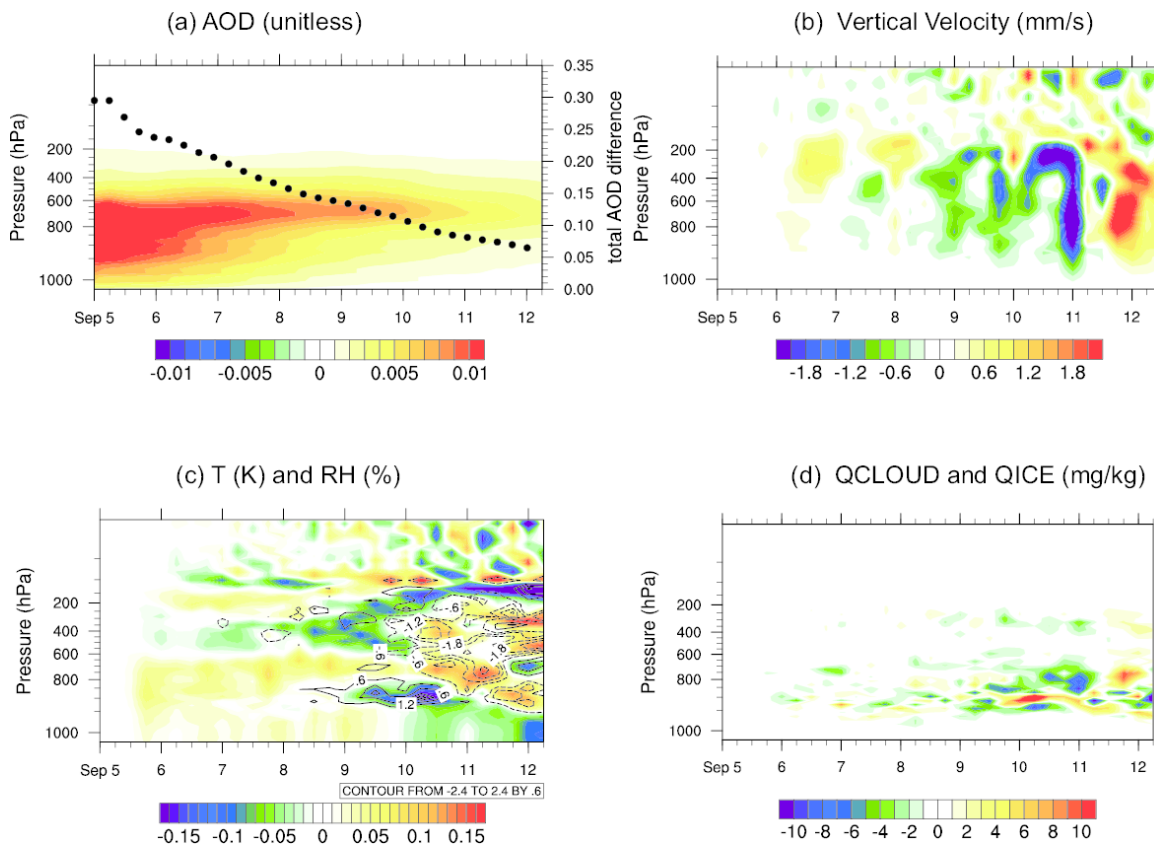

Figure 2. MCR-averaged differences (DA - NO_DA) for (a) AOD, (b) vertical velocity, (c) temperature (color shaded) and relaive humidity (contours), and (d) liquid and ice clouds as a function of height and time.

(a) Cloud
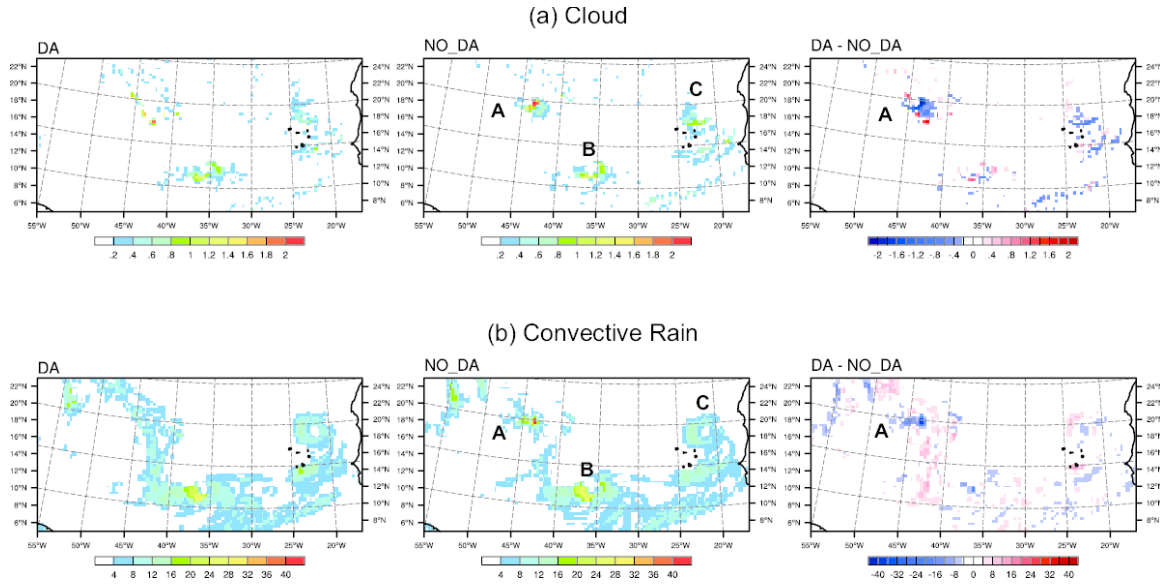
(b) Convective Rain

Figure 3. Spatial distribution and differences of (a) column integrated clouds liquid water path and (b) 114-~120-hr convective rainfall in MCR from two experiments for 120-hr forecast valid at 00UTC 10 Sep. Units: mm.

(a) DA   (b) NO_DA
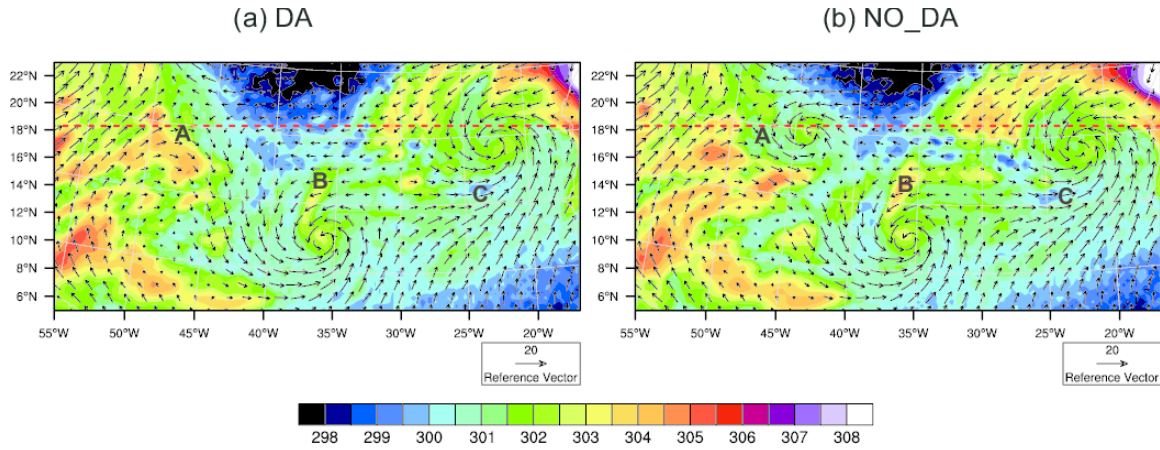
Figure 4. 10-m u-v wind vectors (m/s) and potential temperatures (shaded, K) in MCR for 120-h forecast valid at 00 UTC 10 Sep. The red dashed lines are the west-east cross-section used in Fig. 5.
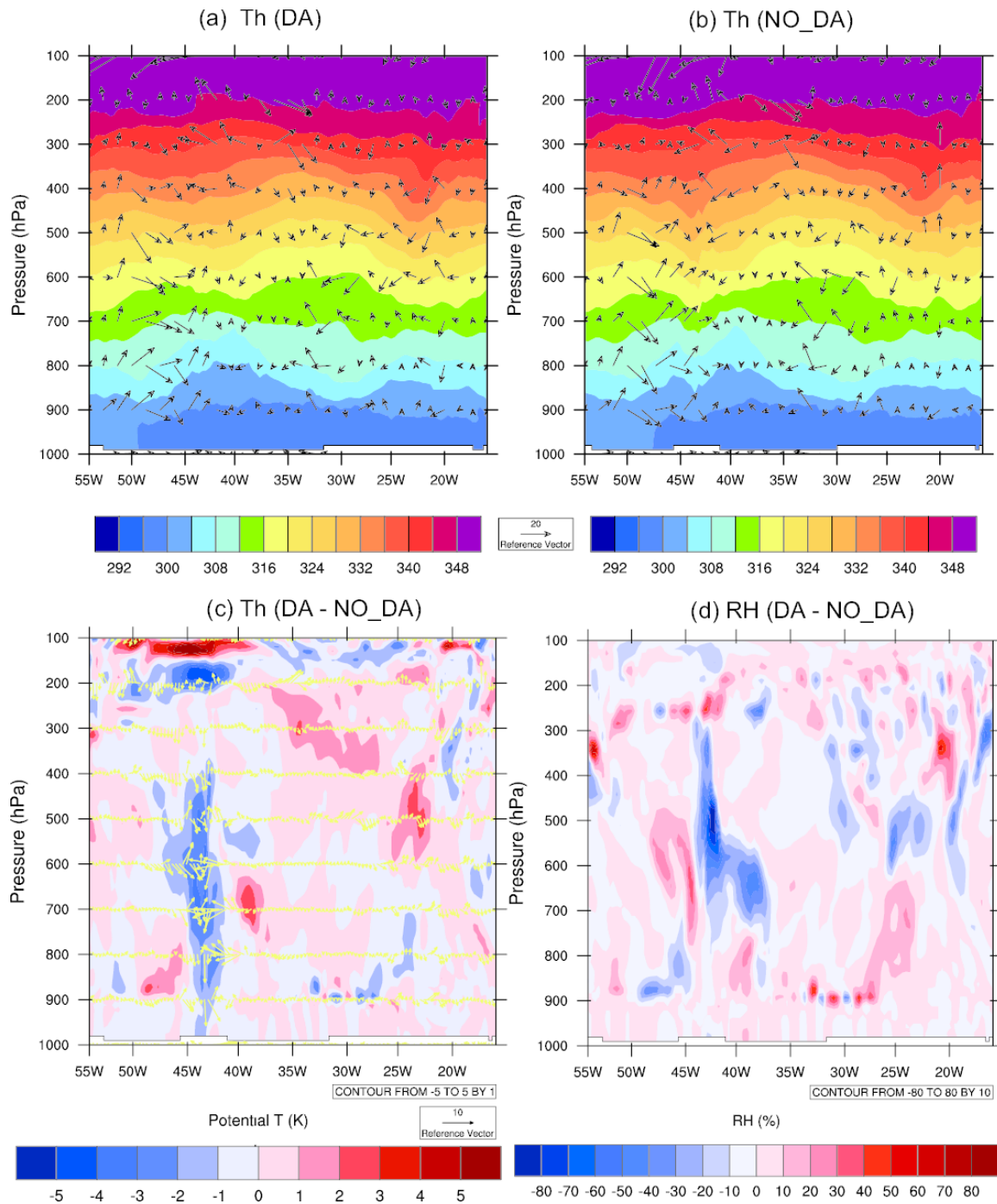
14

Figure 5. Cross sections (along red dashed line in Fig. 6) of (u, 100×W) vectors and potential temperature from the (a) DA and (b) NO_DA experiments as well as (c) the corresponding differences (DA – NO_DA) and (d) relative humidity difference of DA minus NO_DA.
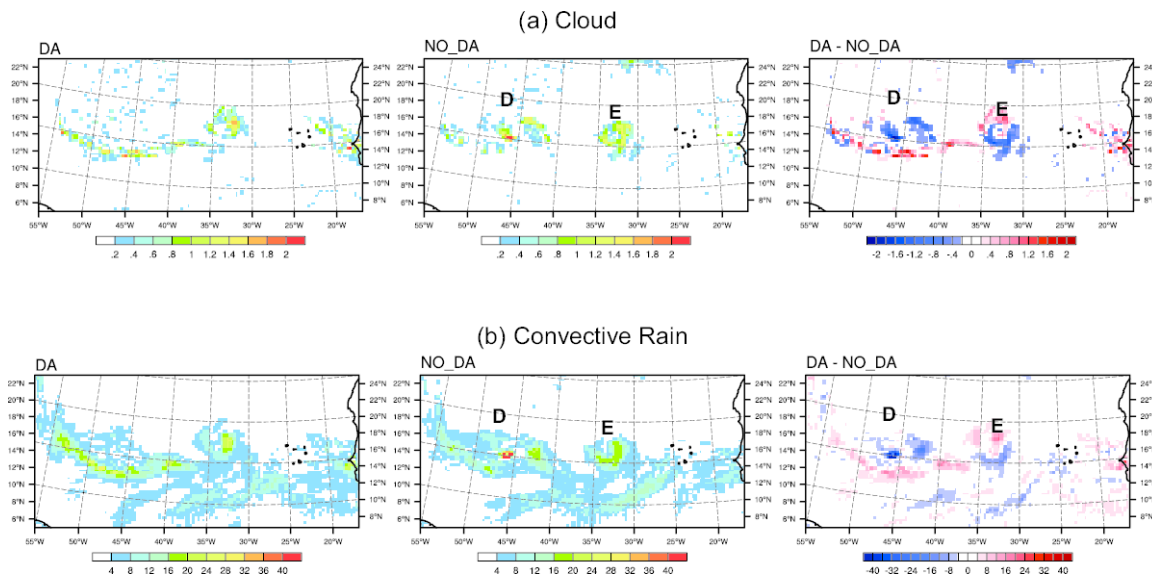
(a) Cloud

(b) Convective Rain

Figure 6. Same as Fig. 3 but for 168-hr forecast valid at 00 UTC 12 Sep.

(a) DA

(b) NO_DA
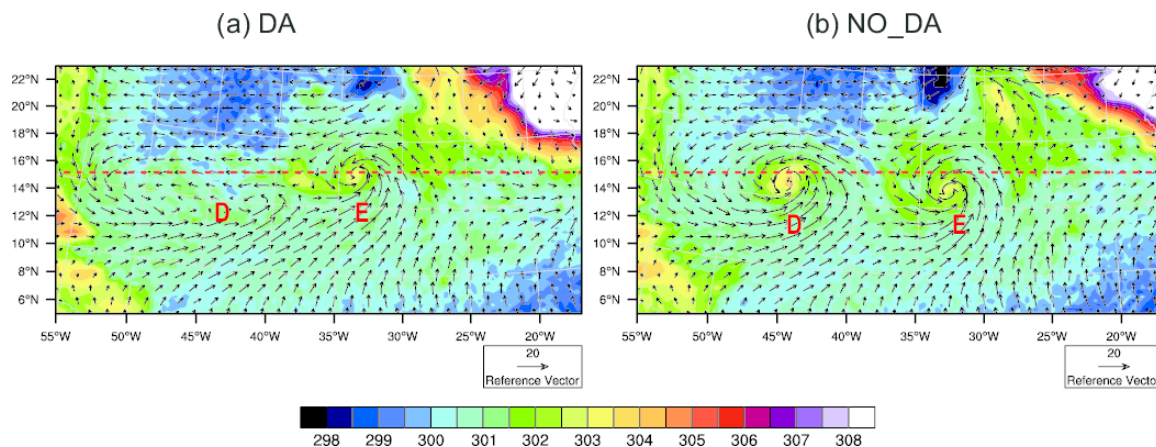
Figure 7. Same as Fig. 4 but for 168-hr forecast valid at 00 UTC 12 Sep. The red dashed lines are the west-east cross section used in Fig. 8.
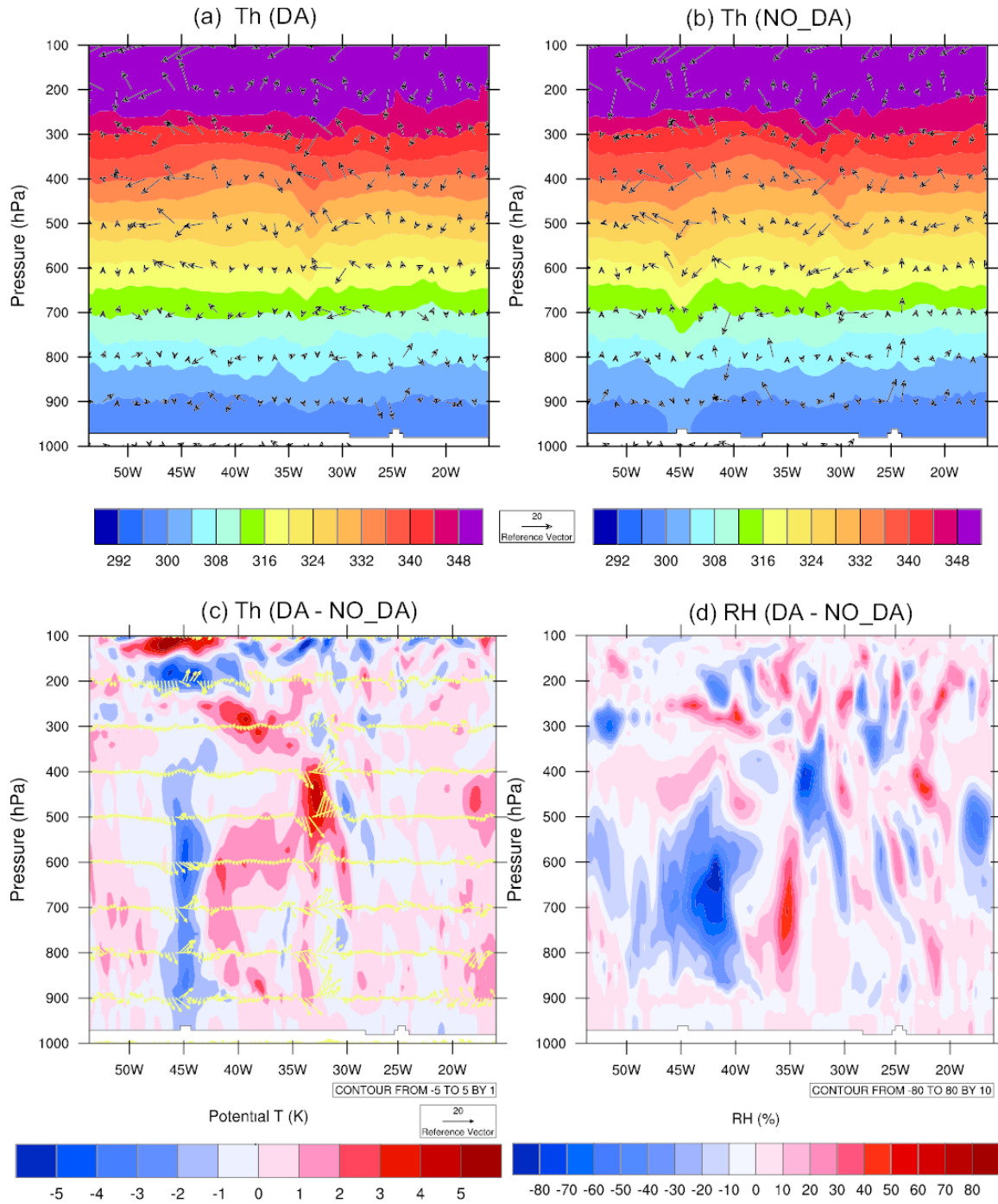
Figure 8. Same as Fig. 5 but for 168-hr forecast valid at 00 UTC 12 Sep. The cross sections are defined as the red dashed lines in Fig. 7.

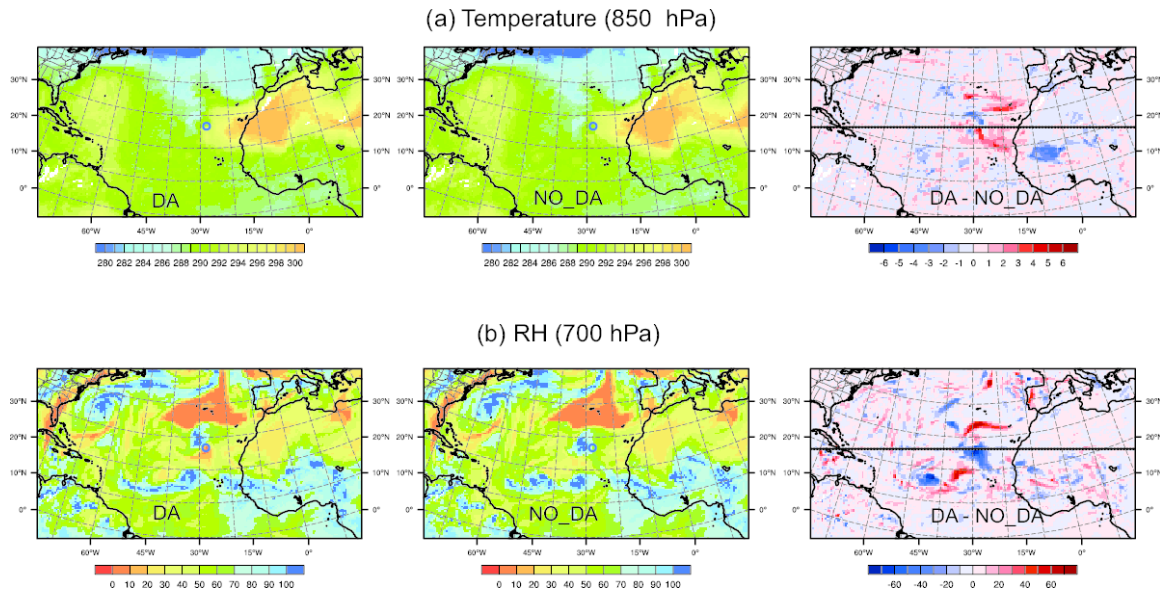(a) Temperature (850 hPa)

(b) RH (700 hPa)

Figure 9. Spatial distributions of (a) 850 hPa temperature (K) and (b) 750 hPa relative humidity (%) from two experiments for 168-hr forecast valid at 00 UTC 12 Sep and the their corresponding differences. The black solid line in the difference field is for the cross sections used in Figure 10.

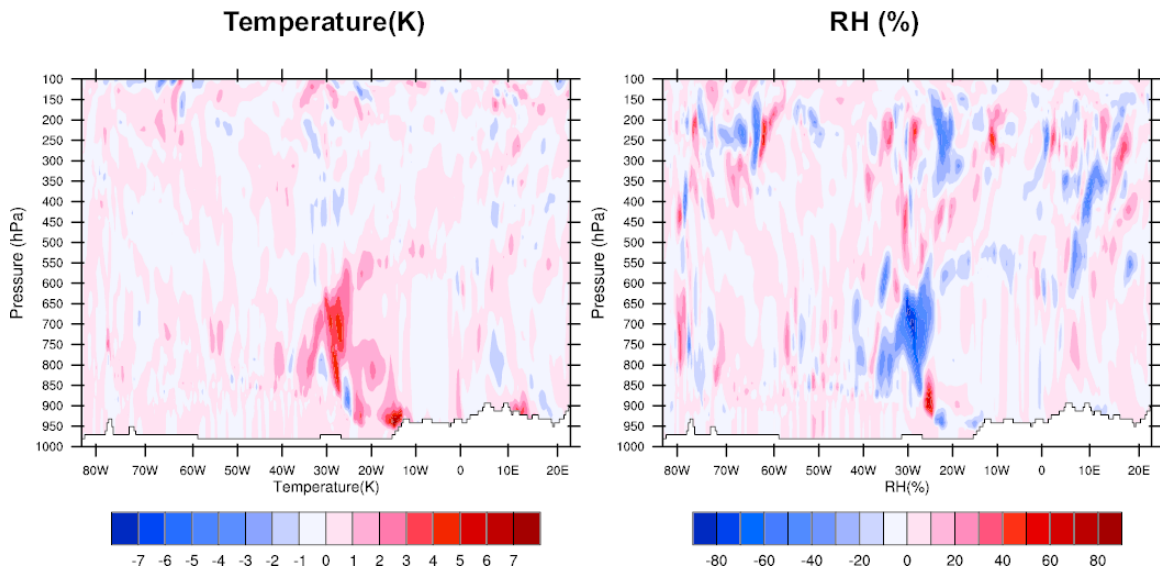Temperature(K)   RH (%)

Figure 10. Cross sections (along black solid line in Figure 9) of (a) temperature difference and (b) relative humidity differences of DA minus NO_DA for 168-hr forecast valid at 00 UTC 12 Sep. 2006.